



Dynamic oxygen migration and reaction over ceria-supported nickel oxides in chemical looping partial oxidation of methane

Rui Liu ^{a,b}, Xianhua Zhang ^{a,b}, Tao Liu ^b, Xian Yao ^b, Zhijian Zhao ^{b,c,d}, Chunlei Pei ^{b,c,d,*}, Jinlong Gong ^{a,b,c,d,**}

^a Joint School of National University of Singapore and Tianjin University, International Campus of Tianjin University, Binhai New City, Fuzhou 350207, China

^b Key Laboratory for Green Chemical Technology of Ministry of Education, School of Chemical Engineering and Technology, Tianjin University, Tianjin 300072, China

^c Collaborative Innovation Center of Chemical Science and Engineering, Tianjin 300072, China

^d Haihe Laboratory of Sustainable Chemical Transformation, Tianjin 300192, China



ARTICLE INFO

Keywords:

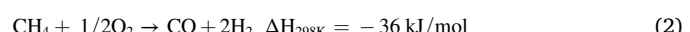
Ni-O-Ce oxygen species
Lattice oxygen migration
Surface reaction mechanism
Chemical looping process
Partial oxidation of methane

ABSTRACT

The oxygen species over oxygen carriers determine the reaction performance in chemical looping partial oxidation of methane (CLPOM). This paper describes the dynamic migration and reaction of oxygen species over ceria-supported NiO oxygen carrier for CLPOM. At initial reaction stage, Ni-O species could be consumed rapidly and cause the full oxidation of methane to CO₂. Afterwards, the active Ni-O-Ce species dominates the methane partial oxidation to promote the syngas yield. It is found that CO formation rate is linearly related with the content of oxygen species over Ni-O-Ce. Furthermore, the lattice oxygen from CeO₂ would migrate through the bulk to complement the consumed Ni-O-Ce oxygen species. Eventually, 5NiO/(40CeO₂-Al₂O₃) exhibit nearly three times as high as methane reaction rate of CeO₂/Al₂O₃ and two times as high as CO formation rate of 5NiO/Al₂O₃. This work provides the comprehensive understanding of transport and reaction mechanism of oxygen species for chemical looping processes.

1. Introduction

The relative abundance of natural gas has resulted in renewed interest in selective methane conversion to generate value-added products from syngas, which is regarded as a mixture of carbon monoxide and hydrogen [1,2]. The syngas with a proper H₂/CO molar ratio is more conductive for the downstream synthesis, such as Fischer-Tropsch process [3,4]. The syngas has been produced commercially via steam reforming (1), partial oxidation (2) and autothermal reforming of methane for several decades [5,6]. Accordingly, these traditional processes suffer from high reaction temperature due to the endothermic nature in reaction (1), and operation safety issues due to the mixing between O₂ and CH₄ in reaction (2) [7,8]. To minimize the energy consumption and environmental impact, new explorations into alternative routes have attracted more attentions.



Chemical looping partial oxidation of methane (CLPOM) is an emerging method to potentially overcome the above-mentioned shortcomings. During CLPOM, CH₄ firstly reacts with oxygen carriers to generate syngas. Subsequently, the reduced oxygen carriers are oxidized through air for oxygen recoverage [9,10]. This technique could eliminate complex gas separation process due to the utilization of air as the oxidant in a separate reactor, and obviate the risk of explosion caused by the mixing of methane and oxygen [11]. Hence, CLPOM is regarded as a potential technique for syngas production.

Various kinds of oxygen carriers have been investigated to enhance the methane oxidation performance of CLPOM, such as ferrite oxides [12,13], tungsten oxides [5,14] and cerium oxides [15,16]. Iron oxides are cost-effective and nontoxic, and have been studied as oxygen carrier

* Corresponding author at: Key Laboratory for Green Chemical Technology of Ministry of Education, School of Chemical Engineering and Technology, Tianjin University, Tianjin 300072, China.

** Corresponding author at: Joint School of National University of Singapore and Tianjin University, International Campus of Tianjin University, Binhai New City, Fuzhou 350207, China.

E-mail addresses: chunlei.pei@tju.edu.cn (C. Pei), jlgong@tju.edu.cn (J. Gong).

candidates extensively [17]. However, the oxygen species in iron-based oxides are so active that the complete oxidation of methane to CO₂ and H₂O dictates [18]. For tungsten oxides, they exhibit superior physical stability and syngas selectivity. Nevertheless, due to the poor reducibility, higher temperatures are required for the utilization of WO₃ lattice oxygen [19]. Ceria-based materials have obtained significant attention in environmental catalysis [20]. They do not only have rich oxygen vacancy and good oxygen release capacity in the Ce⁴⁺/Ce³⁺ redox cycle, but the crystalline structure of CeO₂ can also maintain relatively stable [21]. Moreover, the ceria-based material could oxidize methane selectively and generate the syngas [21]. Therefore, the cerium oxide has been chosen as the oxygen carrier widely in the CLPOM and shown great potentials. However, the absence of C-H activation site limited its direct use in chemical looping methane conversion [22].

Transition/noble metal oxides such as NiO [23–25], Co₂O₃ [26,27], PtO₂ [28,29], and RuO₂ [30,31] are employed as the active sites widely because of the high activity in C-H bonds breaking. Researchers have focused on the exploration of Ni-based catalysts because of the significant availability together with high initial catalytic activity [32]. Therefore, NiO-CeO₂ related materials have become a promising oxygen carrier in CLPOM and received wide attention [33,34]. The lattice oxygen as the central active component involved in CLPOM would determine the reaction performance. Yoshizawa et al. developed DFT method to study the methane activation at an oxygen site interfacing a Ni₄ metal cluster on CeO₂ surface. They found that the interactions between Ni₄ metal clusters and the CeO₂ surface would contribute to the reduction of Ce⁴⁺ cations, promoting the reducibility of the oxygen species at interfacial site and enhancing methane surface activation [35]. Panda et al. developed a highly crystalline NiO/CeO₂ oxygen carrier with various Ni loadings and demonstrated that the interstitial point or surface defects attributed from the under-coordinated oxygen atom in Ce-O-Ni layer would be the possible reason for the good performance [36]. Brandon et al. defined the critical role of the ceria lattice oxygen and explored the surface reaction pathway for methane reforming in detail over Ni/Gd-doped ceria via transient studies. The methane oxidation over Ni/Gd-doped ceria catalyst follows Mars-van Krevelen mechanism, and the reaction is limited by the attainable oxygen concentration on CeO₂ surface [33]. In summary, the current works primarily focus on the study of surface reaction process between CH_x and oxygen species. The lattice oxygen migration pathway from bulk to surface, which also have an essential effect on syngas yield, is still elusive for comprehensively understanding the influence of active oxygen species on CLOPM.

This paper describes the dynamic migration and reaction mechanism of oxygen species over ceria-supported nickel oxide catalysts for CLOPM. The stable and highly active oxygen carrier was synthesized via two-step impregnation method to minimize the formation of NiAl₂O₄ and the Ni²⁺ doping into CeO₂ lattice. The transient chemical species of oxygen carriers and the function of each related active component during redox process were clarified via in situ experimental characterizations. The active Ni-O-Ce oxygen species could devote to the partial oxidation performance and the deactivation was negligible for 5NiO/(40CeO₂-Al₂O₃) over 20 cycles. In situ Raman spectra further demonstrate the involvement of active Ni-O-Ce species in the transformation of CH_x over the surface. Moreover, the dynamic migration pathways of various oxygen species in methane conversion were studied thoroughly via in situ XRD and in situ H₂-TPR for samples pre-activated at different methane pulses.

2. Experimental

2.1. Oxygen carriers preparation

5NiO/(xCeO₂-Al₂O₃) oxygen carriers were synthesized by two-step impregnation. Mixed xCeO₂/Al₂O₃ oxides were obtained by impregnating alumina oxide support (99.9 %, Aladdin biological technology Co., Ltd.) with an aqueous solution of Ce(NO₃)₃·6H₂O (99.95 %, Aladdin

biological technology Co., Ltd.) with appropriate CeO₂ concentration ($x = 10, 20, 30$ and 40 wt %). Subsequently, the samples were dried at 100 °C for overnight. Then, the samples were further grounded to powders and calcined for 3 h at 800 °C in ambient air. Supported NiO oxygen carriers were synthesized by impregnating xCeO₂/Al₂O₃ oxides with aqueous precursor solution of Ni(NO₃)₂·6H₂O (98.0 %, J&K Chemicals Co., Ltd.). Afterwards, it was dried at 100 °C for overnight and calcined in air for 3 h at 800 °C. The theoretical NiO content was 5 wt %. 5NiO/Al₂O₃ were obtained by impregnating alumina oxide with an aqueous solution of Ni(NO₃)₂·6H₂O. Pure CeO₂ were prepared by continuous precipitation. The cerium hydroxides were precipitated by adding NH₃·H₂O solution until the pH value range between 8 and 9. The hydroxides were obtained by centrifugation operation and washed with water thoroughly. Furthermore, the hydroxides were dried and calcined in ambient air to obtain pure CeO₂. The reduced sample as 5NiO/(40CeO₂-Al₂O₃)·H₂ was obtained via reducing 5NiO/(40CeO₂-Al₂O₃) in H₂ flow (10 %H₂/N₂, 40 mL/min) at 800 °C. The reduction time was set as 5 min in order to reduce NiO to Ni completely according to the time evolution of CO₂ selectivity under reaction condition (see details in Fig. 3b).

2.2. Partial oxidation performance tests

Partial oxidation performance tests of oxygen carriers in CLPOM were performed in a fixed bed. 0.8 g of oxygen carriers between 20 and 40 mesh were mixed thoroughly with inert silica (1 mL). Afterwards, the sample was held in a quartz tube with an internal diameter of 8 mm. The isothermal reaction was recorded at 800 °C in methane flow (10 % CH₄/N₂, 40 mL/min) to examine the evolution of methane surface reaction rate and the production rate of CO, H₂ and CO₂. Continuous CLPOM redox tests were done at 800 °C. Oxygen carrier was first reduced by methane reactant (10 % CH₄/N₂, 40 mL/min) for 4 min and further oxidized from air (21 % O₂/N₂, 40 mL/min) for 15 min for oxygen recoverage. N₂ flow (36 mL/min) was conducted for 15 min during the interval between reduction and oxidation to eliminate the direct contact between CH₄ and air during redox steps. The stability test was performed over 40CeO₂/Al₂O₃ and 5NiO/(xCeO₂-Al₂O₃) for 10 continuous cycles. Furthermore, 20 continuous redox process were performed for 5NiO/(40CeO₂-Al₂O₃) to further identify the stability. The outlet gas containing CH₄, H₂, CO, CO₂ and N₂ was analyzed by an on-line gas chromatograph (GC2060, Shanghai Ruimin Instrument). Blank experiments employing only inert silica and Al₂O₃ (0.8 g) were performed under same reaction conditions and showed a rather low contribution (1.7 % and 2.2 % methane conversion) to the current work.

The CH₄ conversion (X_{CH₄}), H₂ (S_{H₂}), CO₂ (S_{CO₂}), CO (S_{CO}) selectivity, H₂/CO (R_{H₂/CO}) ratio, CH₄ reaction rate (r_{CH₄}), CO production rate (r_{CO}) and H₂ production rate (r_{H₂}) are calculated as below:

$$X_{CH_4} = \frac{f_{CH_4, in} - f_{CH_4, out}}{f_{CH_4, in}} \quad (5)$$

$$S_{H_2} = \frac{f_{H_2, out}}{2(f_{CH_4, in} - f_{CH_4, out})} \quad (6)$$

$$S_{CO_2} = \frac{f_{CO_2, out}}{(f_{CH_4, in} - f_{CH_4, out})} \quad (7)$$

$$S_{CO} = \frac{f_{CO, out}}{(f_{CH_4, in} - f_{CH_4, out})} \quad (8)$$

$$R_{H_2/CO} = \frac{f_{H_2, out}}{f_{CO, out}} \quad (9)$$

$$CH_4 \text{ reaction rate : } r_{CH_4} = \frac{X_{CH_4} \times f_{CH_4, in}}{22.4 \times g_{cat}} \quad (10)$$

$$\text{CO production rate} : r_{\text{CO}} = S_{\text{CO}} \times r_{\text{CH}_4} \quad (11)$$

$$\text{H}_2 \text{ production rate} : r_{\text{H}_2} = S_{\text{H}_2} \times r_{\text{CH}_4} \times 2 \quad (12)$$

$$\text{CO}_2 \text{ production rate} : r_{\text{CO}_2} = S_{\text{CO}_2} \times r_{\text{CH}_4} \quad (13)$$

2.3. Characterization

X-ray powder diffraction (XRD) characterization was conducted with Bruker D8 focus type X diffractometer with 2θ values from 15 ° to 85 ° under the scanning step of 8 °/min. The working target during the test process is the copper. The working current and voltage here are 200 mA and 40 kV, respectively.

X-ray photoelectron spectroscopy (XPS) experiment was operated on a Thermo-scientific ESCALAB 250 spectrometer to identify the chemical state over fresh and used oxygen carrier. The excitation source is Al Kα ($\lambda=1486.6 \text{ eV}$) radiation. The influence of charging was calibrated through correcting the C1 s peak (Binding energy: 284.8 eV.).

The elemental composition in oxygen carriers was evaluated via inductively coupled plasma optical emission spectroscopy (ICP-OES). It was developed at a 1.5 kW frequency emission power with a 15.0 L/min plasma airflow. The corresponding oxygen carriers were dissolved in aqueous solution which contains nitric acid, hydrofluoric and hydrochloric acid.

UV-vis spectra with a range from 200 nm to 800 nm were recorded for 5NiO/(xCeO₂-Al₂O₃) (x = 10, 20, 30, 40) and 40CeO₂/Al₂O₃. BaSO₄ was selected as the blank reference on the Shimadzu UV-2550 spectrophotometer.

The reducibility of oxygen carriers was explored through H₂ temperature-programmed reduction (H₂-TPR) on Micromeritics Autochem II 2920. The relevant oxygen carriers (nearly 50 mg) were pretreated under argon flow for 1 h at 300 °C and afterwards were cooled gradually to 100 °C. 10 % H₂ mixed in argon with 30 mL/min was injected to test the reducibility. The reducing temperature was tempted from 100 °C to 1000 °C at a heating rate of 10 °C/min.

Transmission electron microscopy (TEM) was done on JEM-2100 F transmission electron microscope with 100 kV working voltage. To detect the elemental composition, the equipment was equipped with an energy-dispersive X-ray spectros-copy (EDS) detector.

CH₄ temperature-programmed reduction (CH₄-TPR) was conducted with the Micromeritics Autochem II 2920. It was matched with the Hiden QIC-20 mass spectrometer. Oxygen carriers (nearly 200 mg) were swept in argon flow at 300 °C for 1 h. After that, the oxygen carriers were cooled progressively to 100 °C. The experimental temperature was increased from 100 °C to 800 °C with 10 °C/min in a mixing flow (10 % CH₄ in Ar, 30 mL/min). CO₂, CO, H₂, H₂O and CH₄ were identified from the outlet gas through the mass spectrometer (MS).

In situ powder X-ray diffraction (PXRD) patterns was done over a Rigaku Smartlab X-ray diffractometer which employs Cu Kα radiation working at 40 kV and 40 mA. For the temperature program test, oxygen carriers (0.2 g) were heated from 50 °C to 800 °C (5 °C/min) in methane flow (20 % CH₄/Ar, 5 mL/min) and the XRD patterns were recorded for every 50 °C. The structure evolution of 5NiO/(40CeO₂-Al₂O₃) during 10 cycles at isothermal 800 °C was also recorded. The sample (0.2 g) was first heated to 800 °C in Ar flow and the XRD pattern for 'fresh-800 °C' was recorded. Each cycle contains two main steps: methane reduction for 4 min (20 % CH₄/Ar, 5 mL/min) and air oxidation for 15 min (21 % O₂/N₂, 5 mL/min). The XRD diffraction peaks were recorded at the end of methane reduction and air oxidation stage to explore the structure change in CH₄ flow and identify the structural stability of 5NiO/(40CeO₂-Al₂O₃).

TPO profiles of the oxygen carriers after activity test were obtained from the similar apparatus as described for TPR. The spent catalysts were first pretreated at 300 °C for 1 h in argon flow and then cooled down to 100 °C. Finally, TPO profile was done from 100 °C to 800 °C at a heating rate of 10 °C /min under 10 % O₂/He flow (50 mL/min).

Simultaneously, the corresponding mass signal was recorded continuously.

In situ diffuse reflectance infrared Fourier-Transform spectroscopic (DRIFTS) tests were conducted with Thermo Scientific Nicolet iS50 spectrometer. It was equipped with the Harrick Scientific DRIFTS reactor and mercury-cadmium telluride detector which can be further cooled by liquid N₂. To explore the chemical state of surface nickel species during reduction step, CO absorption DRIFTS tests were done for oxygen carriers after methane pretreatment. After the reaction in a mixing flow (CH₄/Ar = 1/4, 25 mL/min) at 600 °C, the oxygen carriers were first maintained in Ar flow to ensure that the lattice oxygen diffusion can reach equilibrium. Afterwards, the samples were cooled down gradually towards 30 °C and the corresponding background was collected after Ar purging (30 mL/min) for 1 h. Afterwards, CO flow (5 mL/min) was injected into the cell and the adsorption of CO molecules on the surface of the oxygen carriers was continued for 30 min. Lastly, the argon was introduced to sweep the CO in reactor and the spectra were recorded until the spectra became stable especially for CO adsorption.

H₂-pulse chemisorption was done to measure the active surface area of Ni species for each oxygen carrier with the same chemisorption analyzer as that in CH₄-TPR. Prior to the experiment, the oxygen carriers (nearly 0.1 g) were reduced in methane flow (10 % CH₄/N₂, 40 mL/min) at 800 °C for 2 min in fixed bed reactor. Afterwards, the treated oxygen carriers were progressively cooled down towards the room temperature. The corresponding methane conversion was recorded. The oxygen carriers after methane reduction were moved into the chemisorption analyzer and pretreated at 50 °C under an Ar flow (30 mL/min). When the baseline was stable, H₂ was pulsed over the oxygen carriers until the peak area of H₂ became stable. The active surface area of Ni species was quantified based on the consumed H₂.

CH₄ pulse reactions were performed similarly as that of H₂-TPR in Micromeritics Autochem II 2920 instrument. Oxygen carriers (nearly 200 mg) were tested for 1 h at 300 °C under argon flow (30 mL/min). Afterwards, the temperature was tempted to 800 °C by 10 °C/min. Subsequently, CH₄ pulse (equal to 0.5082 mL) was introduced into the equipment. The outlet gas was examined through an online mass spectrum.

In situ Raman spectra under 325 nm and 532 nm laser were employed to identify the reaction mechanism of surface oxygen species. During temperature programmed Raman experiments, oxygen carriers were held in nitrogen flow with the temperature ranging from 100 °C to 800 °C. After reaching each aiming temperature, the inlet gas was switched to mixed feed gas (20 % CH₄/Ar, 5 mL/min). After each methane injection process for 5 min, the purging with N₂ for 5 min was done at the same temperature to guarantee enough surface oxygen coverage. Then, isothermal Raman tests were further performed to explore the reaction pathway of each oxygen species. Spectra at various times were collected at 800 °C in mixed feed gas (20 % CH₄/Ar) with 10 mL/min.

In situ H₂-TPR profiles of 5NiO/(40CeO₂-Al₂O₃) pretreated at different methane pluses were employed to identify different kinds of oxygen species resulting in the corresponding oxidation products and explore their oxygen transport pathway. The samples (0.05 g) were treated for 1 h at 300 °C initially in argon flow (30 mL/min). After that the reaction temperature was tempted to 800 °C with 10 °C/min. Then, various amount of CH₄ pulses (0.5082 mL, 20 % CH₄/He) were injected into the reactor. Lastly, the inlet flow was switched into the pure argon flow followed by reducing the operation temperature from 800 °C towards room temperature. Then, in situ H₂-TPR test was tested similarly as that in the H₂-TPR process to analyze the oxygen content.

3. Results and discussion

3.1. Textural properties of fresh oxygen carriers

XRD characterizations of $5\text{NiO}/(x\text{CeO}_2\text{-Al}_2\text{O}_3)$ ($x = 0, 10, 20, 30, 40$) and $\text{CeO}_2/\text{Al}_2\text{O}_3$ fresh oxygen carriers were performed to identify the crystalline structure of oxygen carriers in Fig. 1a. For $40\text{CeO}_2/\text{Al}_2\text{O}_3$ and $5\text{NiO}/(x\text{CeO}_2\text{-Al}_2\text{O}_3)$, the peaks in the diffraction spectra are attributed to cubic CeO_2 phase (JCPDS75-0076) and monoclinic Al_2O_3 phase (JCPDS86-1410), respectively [37,38]. Weak characteristic peak assigned to NiO was observed in the XRD patterns of $5\text{NiO}/(40\text{CeO}_2\text{-Al}_2\text{O}_3)$ due to the high dispersion and small crystalline size ($\sim 6 \text{ nm}$ calculated from Fig. S2 and XRD pattern). Moreover, the crystalline size of NiO would decrease as the loading of CeO_2 increases as shown in Table S1 due to the promoted specific surface area of CeO_2 . The NiO species with small size and strong interaction with CeO_2 achieve better redox performance potentially. The blue shift of CeO_2 diffraction peak is not observed for $5\text{NiO}/(x\text{CeO}_2\text{-Al}_2\text{O}_3)$ in comparison with $40\text{CeO}_2/\text{Al}_2\text{O}_3$, eliminating the doping of Ni^{2+} into CeO_2 lattice. For $5\text{NiO}/\text{Al}_2\text{O}_3$, in addition to a monoclinic Al_2O_3 phase (JCPDS86-1410), a cubic NiAl_2O_4 phase (JCPDS71-0964) appeared [39]. Moreover, as the cerium oxide loading increase, the NiAl_2O_4 would be eliminated gradually due to the enhancement of CeO_2 specific surface area to disperse nickel species.

Raman spectra (Fig. 1b and 1c) showed two characteristic peaks for all the materials at $460\text{-}480 \text{ cm}^{-1}$ and $580\text{-}600 \text{ cm}^{-1}$, assigned to the $\text{F}2g$ vibration model of octahedral local symmetry [40] and oxygen vacancies in CeO_2 lattice, respectively [30,41]. The absence of characteristic bands for nickel oxide also indicated its high dispersion [42]. As shown in Fig. 1b, compared with $40\text{CeO}_2/\text{Al}_2\text{O}_3$, after NiO surface modification, the $\text{F}2g$ peak under 325 nm laser, which is more sensitive

to probe surface information [43], shift downwards notably and the $I_D/I_{\text{F}2g}$ increase, indicating the enhanced surface oxygen vacancy concentration [44]. The concentration of vacancy sites ($I_D/I_{\text{F}2g}$) in CeO_2 bulk almost unchanged, as suggested by $\text{F}2g$ band under 532 nm laser which can detect more sub-surface composition (Table S2) [43]. Thus, it can be preliminarily concluded the nickel species mainly interacted with the surface of cerium oxide.

XPS was further conducted to explore the surface speciation of oxygen carriers. The chemical states of nickel anions are analyzed by $\text{Ni} 2\text{p}$ XPS spectra in Fig. 2a and four kinds of nickel species located at 856.7 eV and 855.4 eV for $5\text{NiO}/(40\text{CeO}_2\text{-Al}_2\text{O}_3)$, together with 855.9 eV and 854.2 eV for $5\text{NiO}/\text{Al}_2\text{O}_3$ [45-47]. Ni^{2+} species loaded on cerium oxide with intimate $\text{Ni}^{2+}\text{-CeO}_2$ interaction has been reported to display a relative higher binding energy in $\text{Ni} 2\text{p}3/2$ spectra [45,47]. Moreover, the following sequence has been found: the $\text{Ni} 2\text{p}3/2$ binding energy of Ni^{2+} species in Ni-O-Ce species (856.6–857.0 eV) > the $\text{Ni} 2\text{p}3/2$ binding energy of NiO with high dispersion > the $\text{Ni} 2\text{p}3/2$ binding energy of NiO aggregate [45,47]. Noteworthily, $5\text{NiO}/(40\text{CeO}_2\text{-Al}_2\text{O}_3)$ oxygen carrier exhibited the strongest interaction between nickel species and CeO_2 surface, generating the Ni-O-Ce species with the highest $\text{Ni} 2\text{p}3/2$ binding energy at 856.7 eV.

The valence states of cerium in $40\text{CeO}_2/\text{Al}_2\text{O}_3$ and $5\text{NiO}/(40\text{CeO}_2\text{-Al}_2\text{O}_3)$ are characterized based on $\text{Ce} 3\text{d}$ XPS spectra (Fig. 2b). The concentration of surface Ce^{3+} species for $40\text{CeO}_2/\text{Al}_2\text{O}_3$ before and after NiO impregnated are quantified by fitting the $\text{Ce} 3\text{d}$ XPS spectra to be 0.141 and 0.259, respectively [48]. The shift of binding energy for Ni^{2+} species and the significant increase of the fraction of Ce^{3+} for $5\text{NiO}/(40\text{CeO}_2\text{-Al}_2\text{O}_3)$ are due to the intimate interaction between NiO and CeO_2 . In other words, a $\text{Ce}^{4+} \leftrightarrow \text{Ce}^{3+}$ redox cycle was attainable for $5\text{NiO}/(40\text{CeO}_2\text{-Al}_2\text{O}_3)$ promoted by surface nickel species. Moreover, the higher atomic ratios of Ni/Ce on $5\text{NiO}/(40\text{CeO}_2\text{-Al}_2\text{O}_3)$ surface

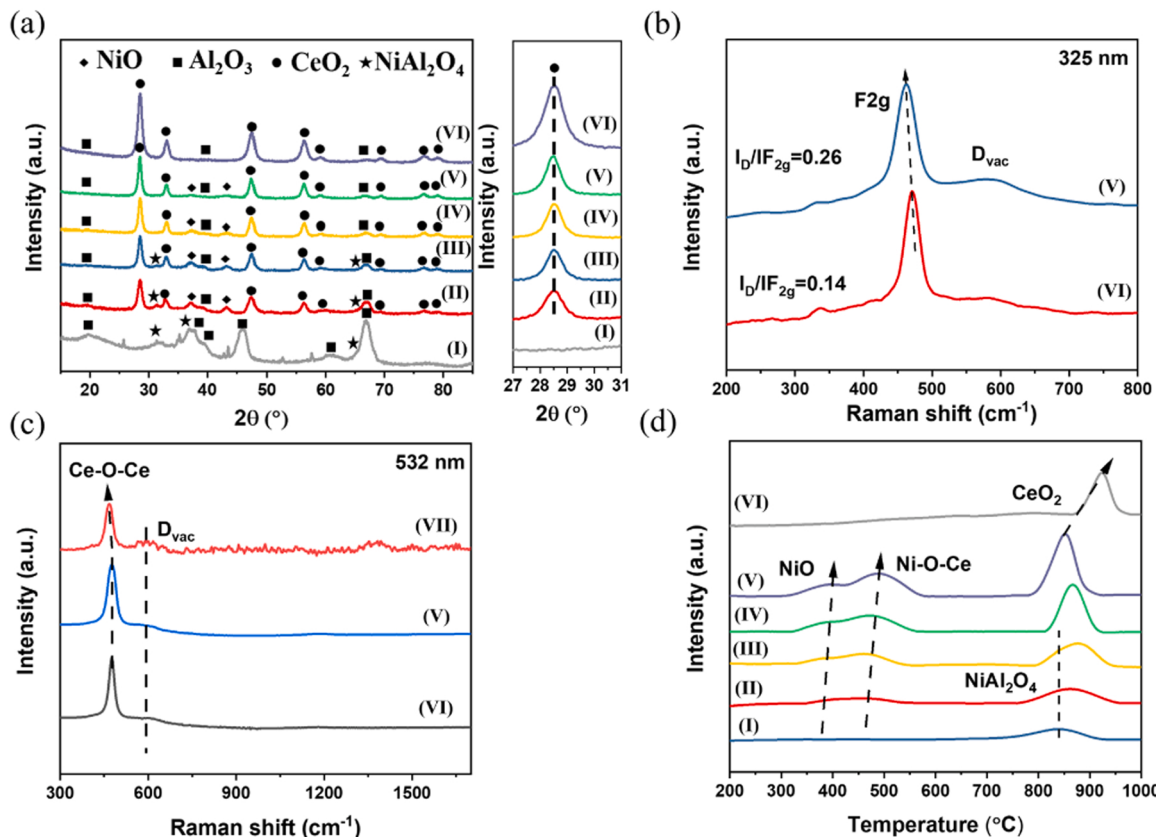


Fig. 1. Physicochemical properties of the $5\text{NiO}/(x\text{CeO}_2\text{-Al}_2\text{O}_3)$ ($x = 0, 10, 20, 30, 40$) and $\text{CeO}_2/\text{Al}_2\text{O}_3$ oxygen carriers. (a) XRD patterns, (b) Raman spectra under 325 nm laser, (c) Raman spectra under 532 nm laser and (d) $\text{H}_2\text{-TPR}$ over different oxygen carriers. ((I) $5\text{NiO}/\text{Al}_2\text{O}_3$, (II) $5\text{NiO}/(10\text{CeO}_2\text{-Al}_2\text{O}_3)$, (III) $5\text{NiO}/(20\text{CeO}_2\text{-Al}_2\text{O}_3)$, (IV) $5\text{NiO}/(30\text{CeO}_2\text{-Al}_2\text{O}_3)$, (V) $5\text{NiO}/(40\text{CeO}_2\text{-Al}_2\text{O}_3)$, (VI) $40\text{CeO}_2/\text{Al}_2\text{O}_3$, (VII) $5\text{NiO}/(40\text{CeO}_2\text{-Al}_2\text{O}_3)$ -reduction).

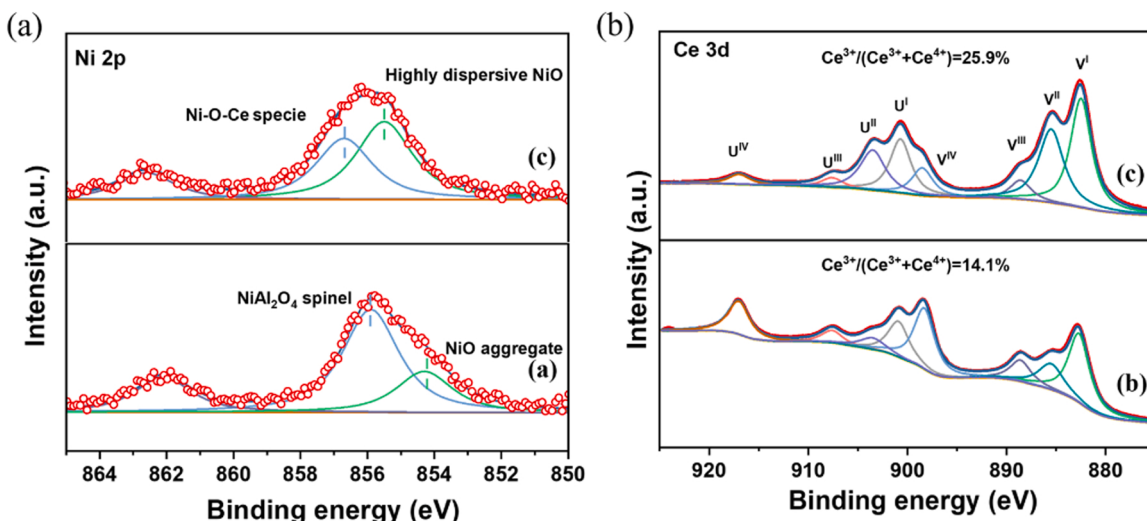


Fig. 2. Electron properties of the 5NiO/(xCeO₂-Al₂O₃) (x = 0, 40) and CeO₂/Al₂O₃ oxygen carriers. XPS spectra of (a) Ni 2p and (b) Ce 3d over different oxygen carriers. ((a) 5NiO/Al₂O₃, (b) 40CeO₂/Al₂O₃, (c) 5NiO/(40CeO₂-Al₂O₃).

relative to the bulk based on the calculation of XPS spectra and ICP (Table 1) could accurately indicate nickel species primarily dispersed on the CeO₂ surface without the generation of NiAl₂O₄. The high oxygen defects for 5NiO/(40CeO₂-Al₂O₃) in Fig. S3 relative to 40CeO₂/Al₂O₃ also suggests that the interplay between Ni²⁺ and CeO₂ species could facilitate the production of surface oxygen vacancies on CeO₂, which would decrease the energy barrier for lattice oxygen migration.

H₂-TPR was developed to further identify the reduction behavior of various oxygen species. For 40CeO₂/Al₂O₃ shown in Fig. 1d, and Fig. S4, the profile can be divided into three different regions: a low temperature region (~670 °C) due to the reduction of small ceria crystallites and/or surface cerium atoms; a medium temperature region (670–850 °C) attributed to the reduction of large/bulk ceria crystallites; and a high-temperature region (>850 °C), assigned to the reduction of Ce⁴⁺ interacted with Al₂O₃ [49]. The reduction temperature for 5NiO/Al₂O₃ was more than 800 °C because of the formation of NiAl₂O₄. UV-vis spectra (Fig. S5) showed that nickel species would preferentially present as NiO and that NiAl₂O₄ was eliminated gradually with the increase of CeO₂ loading. 5NiO/(40CeO₂-Al₂O₃) exhibited three major reduction peaks, corresponded to the reduction of weakly interactive NiO species, strongly interactive NiO species (Ni-O-Ce), and the lattice CeO₂ respectively [50,51]. Particularly, the much higher hydrogen consumption between 400 °C and 550 °C for 5NiO/(40CeO₂-Al₂O₃) compared with that for 40CeO₂/Al₂O₃ below 670 °C which is assigned to the reduction of surface Ce-O oxygen species denotes the reduction peak at 400–550 °C can be mainly attributed to the reduction of NiO strongly interacted with CeO₂ (Ni-O-Ce), besides the negligible amount of surface Ce-O species. As illustrated in Fig. 1d, it is obvious that the hydrogen consumption was promoted as cerium oxide addition increase. Moreover, the promoted hydrogen consumption in lower temperature zone and the downshift of the reduction temperature for bulk Ce-O species for 5NiO/(40CeO₂-Al₂O₃) illustrate the improved oxygen

activity and mobility ascribed to the intimate interaction of Ni-O-Ce.

TEM was employed to identify the morphology of 5NiO/(40CeO₂-Al₂O₃) sample in Fig. S2. The lattice fringe spacing was 0.311 nm and 0.191 nm respectively, which was associated with the CeO₂ (111) facet (JCPDS75-0076) and the NiO (200) facet (JCPDS75-1523) [22]. The close contact between NiO and CeO₂ could be clearly seen, and the Ni-O-Ce oxygen species may serve as oxide centers with dynamic properties due to the Ce⁴⁺/Ce³⁺ and Ni²⁺/Ni redox cycles.

3.2. Redox performance of oxygen carriers

Activity tests were performed for oxygen carriers under methane flow. The influence of the loading of CeO₂ and NiO was studied (detail information was shown in Fig. S6 and Table S1). As illustrated from activity tests, the 5NiO/(40CeO₂-Al₂O₃) shows the most satisfying redox performance. Furthermore, the time evolution of CO, H₂, CO₂ production rates and methane reaction rates were shown in Fig. 3. The H₂ production rate was over 0.3 mmol min⁻¹ g⁻¹ at the beginning for 5NiO/Al₂O₃ calcined at 450 °C in Fig. 3a. Then, it decreased dramatically owing to the insufficient surface oxygen coverage and serious carbon deposition covering the active sites. For 40CeO₂/Al₂O₃ in Fig. 3b, the partial oxidation performance is poor as well due to the lack of surface C-H activation sites [22]. However, for 5NiO/(40CeO₂-Al₂O₃) in Fig. 3c, the high methane reaction rate and syngas selectivity can be both achieved driven by the synergy between surface nickel sites for methane activation and active Ni-O-Ce species for selective oxidation of CH_x. It can be seen the methane conversion has been increased nearly three times higher compared with 40CeO₂/Al₂O₃ sample and the CO selectivity was two times as high as that for 5NiO/Al₂O₃ oxygen carrier. Specifically, the formation of CO₂ primarily occurred in the first two minutes. After that, the partial oxidation stage dominated. As the methane oxidation reaction proceed, the CO selectivity increase first and decrease after 4 min due to the insufficient active oxygen species coverage to oxidize carbon intermediates. Thus, in the following activity test, the reduction time is confined at 4 min to ensure the satisfying syngas yield. Furthermore, to illustrate the excellent reduction behaviors resulted from the strong interactive Ni-O-Ce structure under reaction environment, CH₄-TPR combined with mass spectra was taken in Fig. S7. The lower initial methane activation temperatures for 5NiO/(40CeO₂-Al₂O₃) indicate that the NiO species can be reduced easily and generate the nickel species in metallic state for methane activation. Moreover, the H₂ mass signal was ahead of that of CO. It suggests methane activation and further dehydrogenation to CH_x.

Table 1
XPS and ICP derived atom ratio of various oxygen carriers.

Sample	Ni/Ce _{bulk} ^a	Ni/Ce _{surface} ^b
5NiO/Al ₂ O ₃	0.034(Ni/Al _{bulk})	0.022(Ni/Al _{surface})
5NiO/(40CeO ₂ -Al ₂ O ₃)	0.279	0.415
5NiO/(40CeO ₂ -Al ₂ O ₃)-re	0.277	0.408
5NiO/(40CeO ₂ -Al ₂ O ₃)-1 cycle	0.282	0.416
5NiO/(40CeO ₂ -Al ₂ O ₃)-10 cycle	0.279	0.404

^a : The atom ratio between Ni and Ce/Al was calculated from ICP result.

^b : The atom ratio between Ni and Ce/Al was calculated from XPS result.

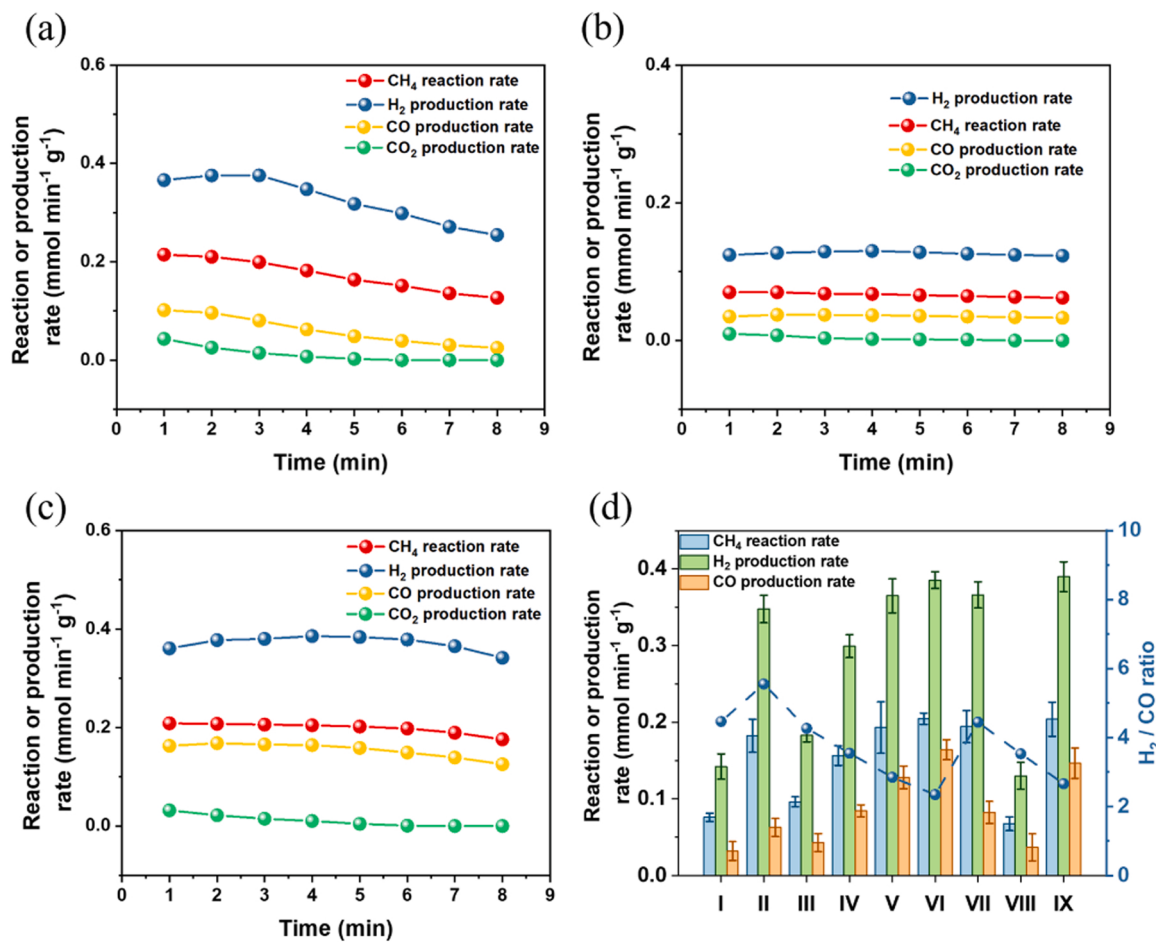


Fig. 3. Activity test of the 5NiO/(xCeO₂-Al₂O₃) ($x = 0, 10, 20, 30, 40$) and CeO₂/Al₂O₃ oxygen carriers. The time evolution of methane reaction rate and CO, H₂, CO₂ production rates of (a) 5NiO/Al₂O₃ calcined at 450 °C, (b) 40CeO₂/Al₂O₃ at 800 °C, (c) 5NiO/(40CeO₂-Al₂O₃), (d) in reduction period of the first cycle, CH₄ conversion, CO and H₂ selectivity, H₂/CO ratio over different oxygen carriers from methane partial oxidation at 800 °C. (I) 5NiO/Al₂O₃, (II) 5NiO/Al₂O₃-450 °C, (III) 5NiO/(10CeO₂-Al₂O₃), (IV) 5NiO/(20CeO₂-Al₂O₃), (V) 5NiO/(30CeO₂-Al₂O₃), (VI) 5NiO/(40CeO₂-Al₂O₃), (VII) 5NiO/Al₂O₃ + 40CeO₂/Al₂O₃, (VIII) 40CeO₂/Al₂O₃, (IX) 5NiO/(40CeO₂-Al₂O₃)-H₂ reduction).

intermediates and H₂ occur preferentially. After that, CO was produced from the CH_x intermediates oxidation via bulk oxygen from CeO₂. The lower CO onset temperature, and the similar initial peak temperatures for H₂ and CO evolved for 5NiO/(40CeO₂-Al₂O₃) suggest the better oxygen activity to match methane activation rate with CH_x oxidation

capacity. The function of active Ni-O-Ce species in the oxidation of CH_x was also explored. The H₂/CO ratio dropped from 5.4 (5NiO/Al₂O₃ calcined at 450 °C) to 4.0 (mechanical mixing that with 40CeO₂/Al₂O₃), and finally to 2.3 for 5NiO/(40CeO₂-Al₂O₃) in Fig. 3d, demonstrating the highly active Ni-O-Ce species induced from the strong interaction

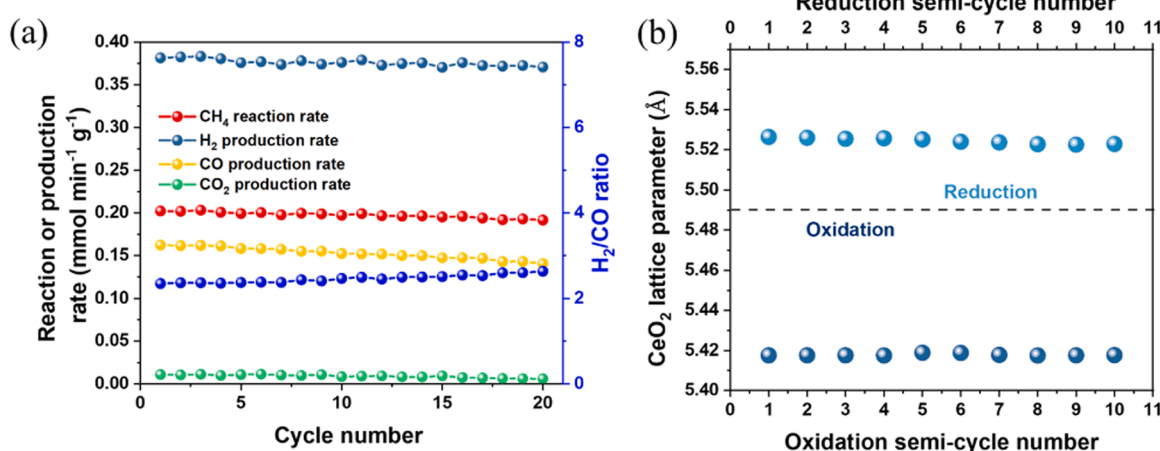


Fig. 4. Stability test of 5NiO/(40CeO₂-Al₂O₃) oxygen carrier. (a) Stability test of 5NiO/(40CeO₂-Al₂O₃) oxygen carrier for CLPOM at 800 °C for 20 cycles, (b) the time evolution of the CeO₂ (111) lattice parameter measured by in situ XRD on 5NiO/(40CeO₂-Al₂O₃) during 10 cycles at 800 °C in CLPOM.

can oxidize the carbon intermediates in time for high syngas yield, in accordance with the results of CH₄-TPR.

3.3. Stability test of oxygen carriers

The stability of 5NiO/(40CeO₂-Al₂O₃) was also studied for the CLOPM. Fig. 4a and S7 show that the deactivation in CO selectivity and methane conversion is negligible. Moreover, the reversible change of CeO₂ (111) lattice parameter in alternating reduction and oxidation steps validated from *in situ* XRD in Fig. 4b and S9 further suggests the excellent structural stability.

Especially, Ni-O-Ce oxygen species plays an essential role in the oxidation of CH_x. Hence, the stability during redox cycles was explored with more detail. In the reduction step, the filamentous carbon decreased for 5NiO/(40CeO₂-Al₂O₃) in Fig. S10, illustrating the close contact between nickel species and CeO₂ can be maintained stable during the reduction process. After the oxidation step, unchanged CeO₂ (111) XRD diffraction peak location (Fig. S11a) and ignorable increase of the bulk oxygen defects concentration in Raman spectra (Table S2) for reacted oxygen carriers could preclude the migration of Ni²⁺ into CeO₂ lattice. Besides, the much higher surface Ni/Ce atom ratio relative to that in bulk in Table 1, and the absence of XPS characteristic peak related to nickel species in NiAl₂O₄ in Fig. S12c, further illustrated the good dispersion of nickel species on CeO₂ surface all along the reaction process. Moreover, the stable proportion of strongly interactive nickel species, Ce³⁺ species, and oxygen defects for reacted oxygen carriers in Fig. S12 and EDS mappings in Fig. S2d again denoted the well retention of active Ni-O-Ce structure in continuous redox cycles.

4. Discussion

4.1. Surface redox reaction mechanism

The deep understanding of the surface reaction mechanism is beneficial to the partial oxidation performance of oxygen carrier. The surface nickel species on CeO₂ was most likely in the metallic state, as the methane reaction rate and syngas yield for 5NiO/(40CeO₂-Al₂O₃) are similar as that of the pre-reduced sample with H₂ (Fig. S13). This agrees with the appearance of nickel species in metallic state as shown in Ni 2p XPS spectra for reduced 5NiO/(40CeO₂-Al₂O₃) in Fig. S14. However, the nickel species at Ni-O-Ce site was potentially in a positive valence state as suggested by the appearance of Ni²⁺ species in intimate contact with ceria surface illustrated from XPS spectra in Fig. S14. It is expected that the consumed Ni-O-Ce species would receive continuous complement by lattice oxygen under the strong interaction condition to stabilize the nickel species in positive state (discuss with more detail in the following section)[52]. Thus, the promoted surface reaction rate for 5NiO/(40-CeO₂-Al₂O₃) displayed in Fig. S13 was potentially due to more available active nickel species sites to promote the C-H activation and enhance the methane conversion, which is consistent with the positive correlation between methane conversion and exposed Ni surface area in Fig. S15.

To further study the effect of Ni-O-Ce oxygen species on methane conversion without the influence of bulk oxygen migration, CH₄ pulse tests were employed to allow enough relaxation time for the bulk oxygen migration. 5NiO/(40CeO₂-Al₂O₃) (Fig. S16b) display much stronger H₂ and CO signals together with lower methane intensity relative to 40CeO₂/Al₂O₃ and 5NiO/Al₂O₃, suggesting the promoted surface reaction between Ni-O-Ce species and methane.

In situ Raman spectroscopy, which can offer useful information of local structure and long-range ordering in sublattices[53], was further performed to discuss the surface reaction mechanism between methane and active oxygen species at 800 °C. To explore the transition pathway of related oxygen species, *in situ* Raman was conducted under intermittent methane flow and recorded every 100 °C with a 5 min interval according to CH₄-pulse results to insure the sufficient lattice oxygen diffusion and surface oxygen coverage in Fig. S17 and S18.

Simultaneously, the variation of oxygen species versus reaction temperature were plotted in Fig. 5a.

With the gradual increase of reaction temperature, the downshift in F2g Raman band frequency and obvious increase of I_D/I_{F2g} shown in Fig. 5a under 532 nm laser revealed the generation of oxygen vacancies in the bulk due to the consumption of CeO₂ lattice oxygen in reducing condition[43]. However, the shift of CeO₂ F2g mode and the variation of surface oxygen defects concentration (I_D/I_{F2g}) of 5NiO/(40CeO₂-Al₂O₃) under 325 nm laser was relatively slow as the temperature evolved[43]. It denotes that the coverage of surface oxygen species can remain stable under intermittent methane flow with lattice oxygen relaxation. To further uncover above phenomenon, *in situ* Raman was performed at isothermal 800 °C in continuous methane flow (Fig. S19), and the evolution profiles of IO_{vac}/IF_{2g} versus temperature were also recorded in Fig. 5b. It is apparent that the increase of surface oxygen vacancy could be observed notably for 5NiO/(40CeO₂-Al₂O₃) during continuous methane injection, confirming its reactivity towards CH_x oxidation. Thus, the relative stabilization of surface oxygen coverage during the temperature program *in situ* Raman experiment was due to the continue replenishment from lattice oxygen after its consumption. In other words, the lattice Ce-O species would be favorable to evolve into surface oxygen species to participate in the oxidation of CH_x to CO continuously. We did similar experiments for a pure CeO₂ oxygen carrier and observe some reduction of the sample as well. However, the formation rate of surface oxygen vacancy at 800 °C was much smaller than that on a 5NiO/(40CeO₂-Al₂O₃) surface under similar conditions, as seen in Fig. 5b. Thus, the addition of NiO to CeO₂ largely facilitates the surface methane activation to carbon intermediates. Afterwards, the carbon intermediates could react with surface oxygen species significantly. Moreover, the increase of surface oxygen defects was more obvious in the latter 5 min with respect to the initial reaction stage for two samples, indicating the insufficient lattice oxygen mobility to replenish the consumed surface oxygen species as methane conversion proceed. Especially, the deactivation behavior is more obvious for pure support, which suggests that 5NiO/(40CeO₂-Al₂O₃) possesses the enhanced oxygen mobility under strong interaction Ni-O-Ce structure. Noteworthily, a linear relationship between the CO formation rate and the Ni-O-Ce oxygen species content calculated from H₂-TPR (the detail calculation method was displayed in Fig. S20 and S21) is observed as depicted in Fig. 5c, which can also confirm the involvement of active Ni-O-Ce species in the oxidation of CH_x to CO, promoting the syngas yield.

The dynamic surface reaction mechanism can be deduced that, 5NiO/(40CeO₂-Al₂O₃) possesses more nano-sized nickel species served as active sites to enhance the methane activation and produce the CH_x* species. Subsequently, the active CH_x* species can react with the active Ni-O-Ce oxygen species instantly to form CO. Besides, more available lattice oxygen below the surface would move to the surface driven by oxygen gradient continuously to complement the consumed surface lattice oxygen species under the condition of strong Ni-O-Ce interaction.

4.2. Dynamic lattice oxygen migration in CLPOM

Since the active oxygen species in redox catalyst undergo dynamic transfer in the CLPOM scheme, detailed insights into the specific oxygen migration pathway can reveal important mechanistic insights. Moreover, the involvement of lattice oxygen in the oxidation of CH_x has already been confirmed from the nearly 2-fold higher I_D/I_{F2g} for methane reduced 5NiO/(40CeO₂-Al₂O₃) relative to fresh sample in Raman spectra.

In situ XRD diffraction patterns were presented to provide a qualitatively understanding into the dynamic lattice oxygen diffusion in reduction step (Fig. S22). For 5NiO/(40CeO₂-Al₂O₃), Ni⁰ species appeared as the reaction temperature went up, indicating the reduction of NiO. During the reduction process, the CeO₂ diffraction peaks shift to

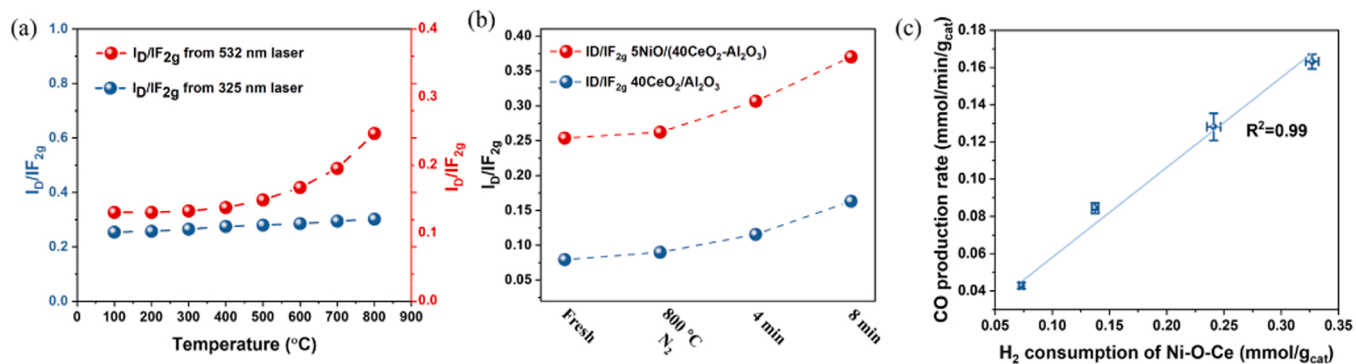


Fig. 5. Surface reaction mechanism between active oxygen species and CH_x in methane conversion. (a) The evolution of oxygen species of $5\text{NiO}/(40\text{CeO}_2\text{-Al}_2\text{O}_3)$ in the methane flow with 325 nm laser (blue line) and 532 nm laser (red line) versus reaction temperature, (b) the evolution of oxygen vacancy content during the methane reaction step at $800\text{ }^\circ\text{C}$ with 325 nm laser associated with time on stream of $5\text{NiO}/(40\text{CeO}_2\text{-Al}_2\text{O}_3)$ and $40\text{CeO}_2/\text{Al}_2\text{O}_3$, (c) the relation between CO formation rate and Ni-O-Ce species content of $5\text{NiO}/(40\text{CeO}_2\text{-Al}_2\text{O}_3)$.

lower angle continuously due to the larger size of Ce^{3+} than Ce^{4+} cation. Thus, the variation in the ceria lattice parameter could be associated with the change of oxygen vacancies content in oxygen carrier directly as displayed in Fig. 6a. $5\text{NiO}/(40\text{CeO}_2\text{-Al}_2\text{O}_3)$ displayed a 4-fold higher evolution rate of CeO_2 (111) lattice parameter and a much deeper reduction degree than bulk CeO_2 , indicating the appreciable oxygen providing capacity. Furthermore, the calculation of the amount of extractable oxygen over CeO_2 in Fig. S23 shows that the reduction degree of CeO_2 for $4\text{NiO}/(40\text{CeO}_2\text{-Al}_2\text{O}_3)$ is nearly 9.58 %, which is much higher compared with that for $40\text{CeO}_2/\text{Al}_2\text{O}_3$ (5.1 %). Hence, a proposal can be made that for $5\text{NiO}/(40\text{CeO}_2\text{-Al}_2\text{O}_3)$, the highly active interfacial oxygen would be consumed immediately in methane flow, and then the vacancies on CeO_2 surface would boost the lattice oxygen migration to participate in methane conversion, promoting the production of syngas.

In order to uncover the lattice oxygen migration pathway quantitatively, $\text{H}_2\text{-TPR}$ of $5\text{NiO}/(40\text{CeO}_2\text{-Al}_2\text{O}_3)$ which was pretreated at different methane pluses were performed in Fig. S24. Simultaneously, the consumption of each oxygen species (Fig. 6b) and the related gas products (Fig. 6c) during methane reaction process were recorded. It should be noted that $\text{O}_2\text{-TPO}$ in Fig. S25 suggests that the influence of carbon deposition in hydrogen flow is negligible. Three kinds of oxygen species were involved in methane oxidation, Ni-O species, Ni-O-Ce species and CeO_2 lattice oxygen (Ce-O species). During the first two pulses, Ni-O species were primarily consumed to generate CO_2 , demonstrated by the superior activity with complete oxidation of methane. Then, the consumption of Ni-O-Ce and Ce-O species were more favorable, leading to the domination of methane partial oxidation products.

It is worth noting that in the third methane pulse, after the depletion of Ni-O bond, the amount of consumed Ni-O-Ce species (9.0×10^{-6} mol/g_{cat}) was much lower than that of Ce-O species (3.01×10^{-5} mol/g_{cat}) as shown in Fig. 6b (the detail calculation method could be found in Fig. S26). However, the poor reducibility toward H_2 in Fig. 1d and the sluggish activity to methane conversion in Fig. 3c could both eliminate the possibility of preferential consumption of CeO_2 lattice oxygen during the reaction process. Therefore, it can be deemed that the Ce-O species could migrate to compensate the active interface oxygen which directly reacts with methane. Therefore, the followed $\text{H}_2\text{-TPR}$ profile cannot observe the loss of Ni-O-Ce species. Particularly, the above oxygen migration pathway could be favorable to make the nickel species located at the Ni-O-Ce site in a more positive valence state during reaction condition, supporting the result of XPS spectra displayed in Fig. S14. As the gradual depletion of cerium bulk oxygen, the attenuation of the oxygen partial pressure gradient (PO_2) between Ce-O and Ni-O-Ce species could degrade the oxygen migration rate of Ce-O to Ni-O-Ce species, and lead to the accelerated consumption of interface oxygen during reduction step. Noteworthily, the proposed oxygen diffusion pathway is also in good agreement with the in situ Raman results to stabilize the interface structure and insure continuous generation of highly active interfacial oxygen species after its consumption. Furthermore, thermodynamic calculation from HSC in Fig. S27 and negligible declination of Ni-O-Ce or Ce-O species under the condition of huge consumption of Ni-O species could eliminate the oxygen migration from other oxygen source to replenish Ni-O species during methane conversion. As for the dynamic oxygen diffusion mechanism, Ni-O-Ce species would accept continuous oxygen replenishment from CeO_2 lattice oxygen to oxidize

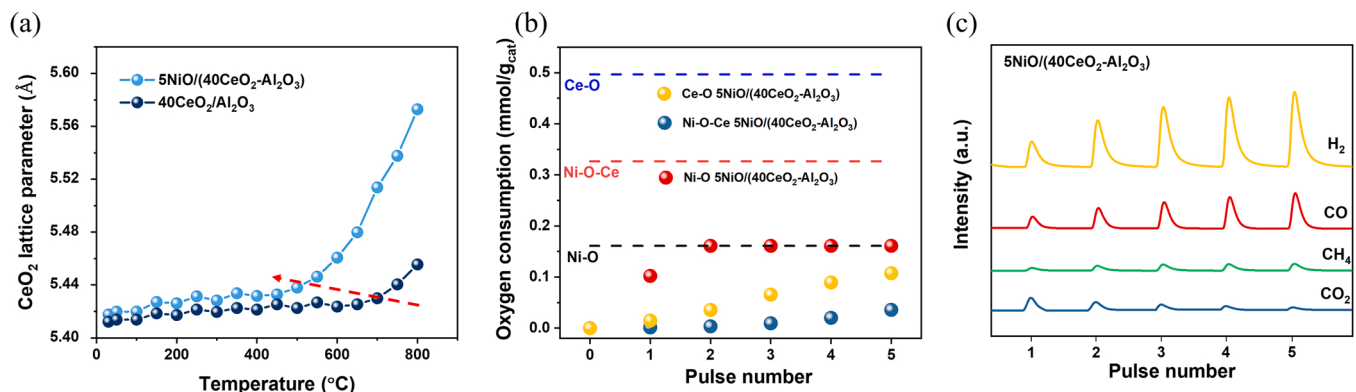


Fig. 6. Lattice oxygen migration pathway of $5\text{NiO}/(40\text{CeO}_2\text{-Al}_2\text{O}_3)$ in methane conversion. (a) The evolution of the lattice parameter of CeO_2 (111) measured in situ XRD at different temperatures in CH_4 stream, (b) the evolution of oxygen consumption at various methane pulses calculated from $\text{H}_2\text{-TPR}$, (c) MS signals at $800\text{ }^\circ\text{C}$ for $5\text{NiO}/(40\text{CeO}_2\text{-Al}_2\text{O}_3)$ with CH_4 pulse. The dash lines in Fig. 6b represent the amount of each oxygen species in fresh oxygen carriers.

carbon intermediates selectively to form CO. These behaviors are beneficial to the excellent syngas yield.

5. Conclusion

In this paper, the ceria-supported nickel oxide was synthesized via the two-step impregnation method for the study of dynamic migration and reaction mechanism of lattice oxygen species for the chemical looping partial oxidation of methane. The specific reaction pathway of three types of oxygen species (Ni-O species, Ni-O-Ce species and Ce-O species) and the corresponding products were further explored using *in situ* characterizations. The results showed that Ni-O species are highly active for the complete oxidation of methane to CO₂, while Ni-O-Ce species are more favorable to dominate in the selective oxidation of methane to syngas. Noteworthily, the lattice Ce-O species could move to surface rapidly under the driven of high oxygen concentration gradient and complement the consumed active Ni-O-Ce species to promote the production of syngas. Subsequently, the active Ni-O-Ce species would be involved in the oxidation of CH_x to suppress the coke formation for 5NiO/(40CeO₂-Al₂O₃) relative to 5NiO/Al₂O₃. In addition, this oxygen carrier showed excellent reaction performance during redox cycles, which suggests the stable structural evolution with the dynamic lattice oxygen migration. This work suggests the importance of investigating the dynamic migration pathway of lattice oxygen and the surface reaction mechanism in methane conversion to aid a deeper understanding of the chemical looping process.

Declaration of Competing Interest

The authors declare that they have no known competing financial interests or personal relationships that could have appeared to influence the work reported in this paper.

Data availability

Data will be made available on request.

Acknowledgments

We acknowledge the National Key R&D Program of China (2021YFA1501302), the National Natural Science Foundation of China (No. 22121004, U20B6002, 22122808, 22208242), the Haihe Laboratory of Sustainable Chemical Transformations and the Program of Introducing Talents of Discipline to Universities (BP0618007) for financial support. This work is supported by the XPLORER PRIZE.

Appendix A. Supporting information

Supplementary data associated with this article can be found in the online version at [doi:10.1016/j.apcatb.2023.122478](https://doi.org/10.1016/j.apcatb.2023.122478).

References

- [1] X. Zhang, F. Zhang, Z. Song, L. Lin, X. Zhao, J. Sun, Y. Mao, W. Wang, Review of chemical looping process for carbonaceous feedstock conversion: rational design of oxygen carriers, *Fuel* 325 (2022).
- [2] S.Z. Sayyed, P.D. Vaidya, Recent insights into the production of syngas and hydrogen using chemical looping-steam reforming (CL-SR), *Ind. Eng. Chem. Res.* 61 (2022) 15015–15029.
- [3] Y. Liu, L. Qin, Z. Cheng, J.W. Goetze, F. Kong, J.A. Fan, L.S. Fan, Near 100% CO selectivity in nanoscaled iron-based oxygen carriers for chemical looping methane partial oxidation, *Nat. Commun.* 10 (2019) 5503.
- [4] Z. Cheng, L. Qin, J.A. Fan, L.-S. Fan, New insight into the development of oxygen carrier materials for chemical looping systems, *Engineering* 4 (2018) 343–351.
- [5] S. Chen, L. Zeng, H. Tian, X. Li, J. Gong, Enhanced lattice oxygen reactivity over Ni-modified WO₃-based redox catalysts for chemical looping partial oxidation of methane, *ACS Catalysis* 7 (2017) 3548–3559.
- [6] M. Tang, K. Liu, D.M. Roddick, M. Fan, Enhanced lattice oxygen reactivity over Fe2O3/Al2O3 redox catalyst for chemical-looping dry (CO₂) reforming of CH₄: synergistic La-Ce effect, *J. Catal.* 368 (2018) 38–52.
- [7] D. Kang, H.S. Lim, M. Lee, J.W. Lee, Syngas production on a Ni-enhanced Fe₂O₃/Al₂O₃ oxygen carrier via chemical looping partial oxidation with dry reforming of methane, *Appl. Energy* 211 (2018) 174–186.
- [8] T. Mattisson, M. Keller, C. Linderholm, P. Moldenhauer, M. Rydén, H. Leion, A. Lyngfelt, Chemical-looping technologies using circulating fluidized bed systems: status of development, *Fuel Process. Technol.* 172 (2018) 1–12.
- [9] X. Yin, L. Shen, S. Wang, B. Wang, C. Shen, Double adjustment of Co and Sr in LaMnO_{3+δ} perovskite oxygen carriers for chemical looping steam methane reforming, *Appl. Catal. B: Environ.* 301 (2022).
- [10] S. Jiang, W. Ding, K. Zhao, Z. Huang, G. Wei, Y. Feng, Y. Lv, F. He, Enhanced chemical looping oxidative coupling of methane by Na-doped LaMnO₃ redox catalysts, *Fuel* 299 (2021).
- [11] D. Kang, M. Lee, H.S. Lim, J.W. Lee, Chemical looping partial oxidation of methane with CO₂ utilization on the ceria-enhanced mesoporous Fe₂O₃ oxygen carrier, *Fuel* 215 (2018) 787–798.
- [12] J. Hu, H. Li, S. Chen, W. Xiang, Enhanced Fe₂O₃/Al₂O₃ oxygen carriers for chemical looping steam reforming of methane with different Mg ratios, *Ind. Eng. Chem. Res.* 61 (2022) 1022–1031.
- [13] K. Yuan, Y. Zheng, K. Li, Z. Yang, H. Wang, Y. Wang, L. Jiang, X. Zhu, Y. Wei, Y. Wang, Enhanced resistance to carbon deposition over La_xCe_{1-x}Fe_xNi_{1-x}O₃ oxygen carrier for chemical looping reforming, *Energy Fuels* 35 (2021) 15867–15878.
- [14] R. Liu, C. Pei, X. Zhang, S. Chen, H. Li, L. Zeng, R. Mu, J. Gong, Chemical looping partial oxidation over FeWO₄/SiO₂ catalysts, *Chin. J. Catal.* 41 (2020) 1140–1151.
- [15] D. Sastre, C.Á. Galván, P. Pizarro, J.M. Coronado, Enhanced performance of CH₄ dry reforming over La_{0.9}Sr_{0.1}FeO₃/YSZ under chemical looping conditions, *Fuel* 309 (2022).
- [16] Y. Khani, N. Safari, F. Bahadoran, S. Soltanali, A. Zamaniyan, High catalytic activity and low coke formation of Ni/Y_xCe_yRu₂O₄ catalysts in the methane reforming process in a microstructure reactor, *Ind. Eng. Chem. Res.* 60 (2021) 9669–9683.
- [17] J. Saupsor, C. Pei, H. Li, S. Wongsakulphasatch, P. Kim-Lohsoontorn, S. Ratchahat, W. Kiatkittipong, S. Assabumrungrat, J. Gong, Bifunctional catalyst NiFe–MgAl for hydrogen production from chemical looping ethanol reforming, *Energy Fuels* 35 (2021) 11580–11592.
- [18] Y. Feng, N. Wang, X. Guo, Reaction mechanism of methane conversion over Ca₂Fe₂O₅ oxygen carrier in chemical looping hydrogen production, *Fuel* 290 (2021).
- [19] L. Zeng, Z. Cheng, J.A. Fan, L.-S. Fan, J. Gong, Metal oxide redox chemistry for chemical looping processes, *Nat. Rev. Chem.* 2 (2018) 349–364.
- [20] S. Kim, J. Lauterbach, E. Sasmanz, Yolk-shell Pt-NiCe@SiO₂ single-atom-alloy catalysts for low-temperature dry reforming of methane, *ACS Catal.* 11 (2021) 8247–8260.
- [21] X. Zhu, H. Wang, Y. Wei, K. Li, X. Cheng, Hydrogen and syngas production from two-step steam reforming of methane using CeO₂ as oxygen carrier, *J. Nat. Gas. Chem.* 20 (2011) 281–286.
- [22] Z. Liu, D.C. Grinter, P.G. Lustemberg, T.D. Nguyen-Phan, Y. Zhou, S. Luo, I. Waluyo, E.J. Crumlin, D.J. Stacchiola, J. Zhou, J. Carrasco, H.F. Busnengo, M. V. Ganduglia-Pirovano, S.D. Senanayake, J.A. Rodriguez, Dry reforming of methane on a highly-active Ni-CeO₂ catalyst: effects of metal-support interactions on C-H bond breaking, *Angew. Chem. Int. Ed. Engl.* 55 (2016) 7455–7459.
- [23] B. Sellers-Anton, E. Bailon-Garcia, A. Cardenas-Arenas, A. Davo-Quinonero, D. Lozano-Castello, A. Bueno-Lopez, Enhancement of the generation and transfer of active oxygen in Ni/CeO₂ catalysts for soot combustion by controlling the Ni-ceria contact and the three-dimensional structure, *Environ. Sci. Technol.* (2020).
- [24] K. Bu, J. Deng, X. Zhang, S. Kuboon, T. Yan, H. Li, L. Shi, D. Zhang, Promotional effects of B-terminated defective edges of Ni/boron nitride catalysts for coking- and sintering-resistant dry reforming of methane, *Appl. Catal. B: Environ.* 267 (2020).
- [25] C. Ruan, Z.-Q. Huang, J. Lin, L. Li, X. Liu, M. Tian, C. Huang, C.-R. Chang, J. Li, X. Wang, Synergy of the catalytic activation on Ni and the CeO₂–TiO₂/Ce₂Ti₂O₇ stoichiometric redox cycle for dramatically enhanced solar fuel production, *Energy Environ. Sci.* 12 (2019) 767–779.
- [26] X. Wang, B. Jin, R. Feng, W. Liu, D. Wang, X. Wu, S. Liu, A robust core-shell silver soot oxidation catalyst driven by Co₃O₄: effect of tandem oxygen delivery and Co₃O₄–CeO₂ synergy, *Appl. Catal. B: Environ.* 250 (2019) 132–142.
- [27] Z. Wu, B. Yang, S. Miao, W. Liu, J. Xie, S. Lee, M.J. Pellin, D. Xiao, D. Su, D. Ma, Lattice strained Ni–Co alloy as a high-performance catalyst for catalytic dry reforming of methane, *ACS Catalysis* 9 (2019) 2693–2700.
- [28] B.T. Egelske, J.M. Keels, J.R. Monnier, J.R. Regalbuto, An analysis of electroless deposition derived Ni–Pt catalysts for the dry reforming of methane, *J. Catal.* 381 (2020) 374–384.
- [29] Z. Xie, B. Yan, S. Kattel, J.H. Lee, S. Yao, Q. Wu, N. Rui, E. Gomez, Z. Liu, W. Xu, L. Zhang, J.G. Chen, Dry reforming of methane over CeO₂-supported Pt–Co catalysts with enhanced activity, *Appl. Catal. B: Environ.* 236 (2018) 280–293.
- [30] M.A. Naeem, P.M. Abdala, A. Armutlulu, S.M. Kim, A. Fedorov, C.R. Müller, Exsolution of metallic Ru nanoparticles from defective, fluorite-type solid solutions Sm₂Ru_xCe_{2-x}O₇ to impart stability on dry reforming catalysts, *ACS Catal.* (2020) 1923–1937.
- [31] S. Das, R. Gupta, A. Kumar, M. Shah, M. Sengupta, S. Bhandari, A. Bordoloi, Facile synthesis of ruthenium decorated Zr_{0.5}Ce_{0.5}O₂ nanorods for catalytic partial oxidation of methane, *ACS Appl. Nano Mater.* 1 (2018) 2953–2961.
- [32] Y. Tang, Y. Wei, Z. Wang, S. Zhang, Y. Li, L. Nguyen, Y. Li, Y. Zhou, W. Shen, F. F. Tao, P. Hu, Synergy of single-atom Ni₁ and Ru₁ sites on CeO₂ for dry reforming of CH₄, *J. Am. Chem. Soc.* 141 (2019) 7283–7293.

- [33] M. Ouyang, P. Boldrin, R.C. Maher, X. Chen, X. Liu, L.F. Cohen, N.P. Brandon, A mechanistic study of the interactions between methane and nickel supported on doped ceria, *Appl. Catal. B: Environ.* 248 (2019) 332–340.
- [34] N. Wang, K. Shen, L. Huang, X. Yu, W. Qian, W. Chu, Facile route for synthesizing ordered mesoporous Ni-Ce-Al oxide materials and their catalytic performance for methane dry reforming to hydrogen and syngas, *ACS Catal.* 3 (2013) 1638–1651.
- [35] R.K. Singha, Y. Tsuji, M.H. Mahyuddin, K. Yoshizawa, Methane activation at the metal-support interface of Ni₄-CeO₂(111) catalyst: a theoretical study, *J. Phys. Chem. C* 123 (2019) 9788–9798.
- [36] P. Pal, R.K. Singha, A. Saha, R. Bal, A.B. Panda, Defect-induced efficient partial oxidation of methane over nonstoichiometric Ni/CeO₂ nanocrystals, *J. Phys. Chem. C* 119 (2015) 13610–13618.
- [37] C.M. Damaskinos, J. Zavašnik, P. Djinović, A.M. Efstatithou, Dry reforming of methane over Ni/Ce_{0.8}Ti_{0.2}O_{2-δ}: the effect of Ni particle size on the carbon pathways studied by transient and isotopic techniques, *Appl. Catal. B: Environ.* 296 (2021).
- [38] A.S. Al-Fatesh, Y. Arafat, S.O. Kasim, A.A. Ibrahim, A.E. Abasaeed, A.H. Fakheeha, In situ auto-gasification of coke deposits over a novel Ni-Ce/W-Zr catalyst by sequential generation of oxygen vacancies for remarkably stable syngas production via CO₂-reforming of methane, *Appl. Catal. B: Environ.* 280 (2021).
- [39] X. Gao, Z. Ge, G. Zhu, Z. Wang, J. Ashok, S. Kawi, Anti-coking and anti-sintering Ni/Al₂O₃ catalysts in the dry reforming of methane: recent progress and prospects, *Catalysts* 11 (2021).
- [40] Y. Han, M. Tian, C. Wang, Y. Kang, L. Kang, Y. Su, C. Huang, T. Zong, J. Lin, B. Hou, X. Pan, X. Wang, Highly active and anticoke Ni/CeO₂ with ultralow ni loading in chemical looping dry reforming via the strong metal–support interaction, *ACS Sustain. Chem. Eng.* 9 (2021) 17276–17288.
- [41] S. Bai, F. Liu, B. Huang, F. Li, H. Lin, T. Wu, M. Sun, J. Wu, Q. Shao, Y. Xu, X. Huang, High-efficiency direct methane conversion to oxygenates on a cerium dioxide nanowires supported rhodium single-atom catalyst, *Nat. Commun.* 11 (2020).
- [42] X. Meng, Y. Du, X. Gao, Face-centered cubic p-type NiO films room-temperature prepared via direct-current reactive magnetron sputtering—Influence of sputtering power on microstructure, optical and electrical behaviors, *Phys. B: Condens. Matter* 579 (2020).
- [43] H. Zhang, J. Cai, Y. Wang, M. Wu, M. Meng, Y. Tian, X. Li, J. Zhang, L. Zheng, Z. Jiang, J. Gong, Insights into the effects of surface/bulk defects on photocatalytic hydrogen evolution over TiO₂ with exposed {001} facets, *Appl. Catal. B: Environ.* 220 (2018) 126–136.
- [44] M. Gupta, A. Kumar, A. Sagdeo, P.R. Sagdeo, Doping-induced combined fano and phonon confinement effect in La-doped CeO₂: Raman spectroscopy analysis, *J. Phys. Chem. C* 125 (2021) 2648–2658.
- [45] X. Zhang, R. You, D. Li, T. Cao, W. Huang, Reaction sensitivity of ceria morphology effect on Ni/CeO(2) catalysis in propane oxidation reactions, *ACS Appl. Mater. Interfaces* 9 (2017) 35897–35907.
- [46] X. Cai, Y. Cai, W. Lin, Autothermal reforming of methane over Ni catalysts supported over ZrO₂-CeO₂-Al₂O₃, *J. Nat. Gas. Chem.* 17 (2008) 201–207.
- [47] M. Li, A.C. van Veen, Tuning the catalytic performance of Ni-catalysed dry reforming of methane and carbon deposition via Ni-CeO₂-interaction, *Appl. Catal. B: Environ.* 237 (2018) 641–648.
- [48] A.L.A. Marinho, F.S. Toniolo, F.B. Noronha, F. Epron, D. Duprez, N. Bion, Highly active and stable Ni dispersed on mesoporous CeO₂-Al₂O₃ catalysts for production of syngas by dry reforming of methane, *Appl. Catal. B: Environ.* 281 (2021).
- [49] A. Piras, S. Colussi, A. Trovarelli, V. Sergio, J. Llorca, R. Psaro, L. Sordelli, Structural and morphological investigation of ceria-promoted Al(2)O(3) under severe reducing/oxidizing conditions, *J. Phys. Chem. B* 109 (2005) 11110–11118.
- [50] W. Liu, W. Wang, K. Tang, J. Guo, Y. Ren, S. Wang, L. Feng, Y. Yang, The promoting influence of nickel species in the controllable synthesis and catalytic properties of nickel–ceria catalysts, *Catal. Sci. Technol.* 6 (2016) 2427–2434.
- [51] L. Wang, H. Liu, Y. Liu, Y. Chen, S. Yang, Influence of preparation method on performance of Ni-CeO₂ catalysts for reverse water-gas shift reaction, *J. Rare Earths* 31 (2013) 559–564.
- [52] B. Solsona, P. Concepción, S. Hernández, B. Demicol, J.M.L. Nieto, Oxidative dehydrogenation of ethane over NiO-CeO₂ mixed oxides catalysts, *Catal. Today* 180 (2012) 51–58.
- [53] D.L. Drey, E.C. O’Quinn, T. Subramani, K. Lilova, G. Baldinozzi, I.M. Gussev, A. F. Fuentes, J.C. Neufeld, M. Everett, D. Sprouster, A. Navrotksy, R.C. Ewing, M. Lang, Disorder in Ho₂Ti_{2-x}Zr_xO₇: pyrochlore to defect fluorite solid solution series, *RSC Adv.* 10 (2020) 34632–34650.